Characteristics of electromagnetically accelerated plasma flow in an externally applied magnetic field

doi: 10.1063/1.2773701

Characteristics of electromagnetically accelerated plasma flow in an externally applied magnetic field

Hiroyuki Tobari,[a] Akira Ando, Masaaki Inutake, and Kunihiko Hattori
Department of Electrical Engineering, Graduate School of Engineering, Tohoku University, 6-6-05, Aoba-yama, Sendai 980-8579, Japan

(Received 5 January 2007; accepted 27 July 2007; published online 26 September 2007)

In order to clarify the acceleration mechanism of applied-field magneto-plasma-dynamic arcjet (MPDA) plasma, the spatial profiles of the flow field and electromagnetic field near the outlet of the MPDA were measured using magnetic probes and the spectroscopic method. The plasma current densities and Lorentz forces acting on the plasma were evaluated experimentally. It was found that the azimuthal rotation of the exhausted plasma in the applied magnetic field is determined by a balance among the $E \times B$ drift, the diamagnetic drift, and the centrifugal force drift. Three components of the Lorentz force, i.e., the radial, the azimuthal, and the axial, were measured experimentally for the first time. The radial component F_r was dominant among the three components and the axial one (F_z) was weakened by the deceleration force, which spontaneously appeared in the applied-field MPDA plasma due to a diamagnetic effect of the high-beta plasma. It was demonstrated that the deceleration force can be converted to an acceleration force in an externally applied diverging field. © *2007 American Institute of Physics*. [DOI: 10.1063/1.2773701]

I. INTRODUCTION

Recently, fast-flowing plasmas have been recognized to play an important role in fusion plasma, space plasma, and Earth's magnetosphere plasma. They have been associated with various magnetohydrodynamic phenomena, such as astronomical jets, solar flares, particle acceleration, auroras, and the Earth's bow-shock formation. The remarkable development of diagnostic instruments has enabled us to understand the physical mechanisms behind those phenomena. Plasma flow has also attracted much attention in fusion research because of its close relation to the formation of transport barriers and the zonal flow.[1]

As in space plasma and fusion plasma research, the production and control of fast-flowing plasma is important in other types of research such as space propulsion with electric propulsion (EP) systems.[2] These systems require high-enthalpy plasma flows induced by electric power, which ionizes the propellant gas and accelerates it by electrothermal, electrostatic, or electromagnetic means. Recently, EP systems have been utilized not only for attitude and/or orbital control of satellites but for the main engines in interplanetary transportation. As the ionized propellant is exhausted backward from the EP thruster with a velocity of several tens of kilometers per second, which is one order higher than that produced by conventional chemical rockets, its specific impulse becomes high and the consumption rate of the propellant is low. These features enable long-term space missions, such as the asteroid-sample-return mission (MUSES-C project) of JAXA, Japan,[3] where four ion engines are installed on the spacecraft HAYABUSA as its main engines.

A magneto-plasma-dynamic arcjet (MPDA),[2,4–6] which has coaxial electrodes consisting of a central cathode rod and an annular anode, produces a high-enthalpy plasma. It has been developed as one of the representative space thrusters with relatively large thrust as far as EP systems are concerned, and is expected to be utilized in space transportation. With a high arc current (more than 1 kA), the plasma produced in the MPDA is accelerated electromagnetically by the Lorentz force ($j_r \times B_\theta$) in the axial direction, where j_r is the radial discharge current and B_θ is the self-induced azimuthal magnetic field. In order to enhance the acceleration performance of MPDAs, it has been proposed to operate with various types of externally applied magnetic field. When an axial magnetic field B_z is applied to an MPDA, the interaction between j_r and B_z generates an azimuthal acceleration force, which results in an azimuthal plasma rotation in addition to the axial flow. A diverging magnetic configuration enables the conversion of the rotational momentum into an axial one and enhances the plasma flow velocity. In addition, the Lorentz force induced by azimuthally induced Hall current j_θ and the radial component of the diverging magnetic field B_r accelerate the plasma axially (Hall acceleration). The plasma rotation induced by B_z reduces the concentration of the discharge current on the electrodes and effectively prevents electrode erosion.

Several numerical analyses and experimental efforts have been carried out regarding the acceleration mechanism of applied-field MPDA plasmas in order to improve the plasma flow parameters. Seal and Hassan have analyzed a plasma flow quasi-one-dimensionally, taking into account various effects such as the Hall effect and Joule heating under a nonequilibrium conditions.[7] In their analysis, however, the effects of the self-induced field and the conversion of the rotational momentum into an axial one in the magnetic nozzle were not taken into consideration. Krülle has attempted a two-dimensional analysis of an MPDA plasma plume in an applied field at low current density and a low

[a]Present affiliation: Japan Atomic Energy Agency, Mukouyama 801-1, Naka, Ibaraki 311-0193, Japan. Electronic mail: tobari.hiroyuki@jaea.go.jp

mass-flow rate.[8] He assumed that the plasma was fully ionized and the self-induced field was much weaker than the applied field. His analysis showed that a considerable fraction of the total thrust was generated by the pressure force, which balanced with the $j \times B$ force in the radial direction. Tanaka and Kimura have investigated numerically the applied-field acceleration mechanism using two-dimensional electromagnetic equations and quasi-one-dimensional fluid equations.[9] They have shown that the azimuthal motion of the plasma is converted into a axial one in the magnetic nozzle; this process is called magnetic swirl acceleration. The Hall acceleration and the swirl acceleration occurred in a slowly diverging applied magnetic field.

In previous experimental studies, MPDAs have been operated using an applied field formed by simple solenoid coils or permanent magnets, and increased thrust has been observed by means of a thrust stand.[10–13] The mechanism of thrust increase, however, has not been clarified sufficiently, either experimentally or theoretically. It is essential for the clarification of the acceleration mechanism of applied-field MPDA plasmas to precisely measure the flow field and electromagnetic force (Lorentz force) field working on the plasma since they are closely related to the self-field acceleration, the swirl acceleration, and the Hall acceleration. The contribution of each component, as well as that of the gas dynamic acceleration, to the thrust must be elucidated.

In this paper, characteristics of an MPDA plasma flow in an externally applied magnetic field are reported. In Sec. II, the experimental apparatus is described. In Sec. III A, azimuthal plasma rotation in a uniform applied field is analyzed using the force balance equation. In Sec. III B, the saturation phenomena related to the flow Mach number are presented. In Sec. III C, spatial profiles of Lorentz force densities working on the plasma flow are evaluated by the direct measurement of magnetic field in the plasma flow, and the desirable applied-field configuration for efficient plasma acceleration is discussed.

II. EXPERIMENTAL APPARATUS

A. HITOP device and MPDA plasma source

The experiments were performed in the high-density Tohoku plasma (HITOP) device of Tohoku University.[16–18] The HITOP device consists of a large cylindrical vacuum chamber (diameter $D=0.8$ m, length $L=3.3$ m) and external magnetic coils, as shown in Fig. 1. Various types of magnetic field configurations can be formed by adjusting each coil current and maximum strength of uniform magnetic field reaches at this time is 1 kG using the existing power supplies for the present set of magnetic coils. The chamber was evacuated by two turbomolecular pumps, each operating at a pumping speed of 1500 l/s.

A high-power, quasi-steady MPDA is installed at one end of the HITOP device. It has a coaxial structure with a center tungsten rod cathode (10 mm in diameter) and an annular molybdenum anode (30 mm in diameter). A schematic view of the MPDA is shown in Fig. 2. One discharge continues for 1 ms quasi-steadily with a pulse-forming-network (PFN) power supply. The discharge current I_d can be controlled by varying the charging voltage of the capacitor bank in the PFN power supply. The repetition rate of the discharges depends on the charging time of the capacitors and is typically one shot per minute. The maximum I_d value is 10 kA, with a typical discharge voltage of 150–200 V in present experiments. Helium gas was used as the working gas and was supplied to the discharge region quasi-steadily for 3 ms by a fast-acting gas valve. Although instabilities in the MPDA plasma was observed especially in high discharge current and low magnetic field regime,[14,15] they were found to be current-driven instabilities (helical kink instabilities) and a control of the safety factor q $(=4\pi^2 a^2 B_z/\mu_0 L I_z)$ of more than unity enables stable discharges without such instabilities, where a and L are a radius and a length of a plasma column, respectively, and I_z is a total axial plasma current in a plasma column. Experiments were performed in the condition without occurrence of such instabilities.

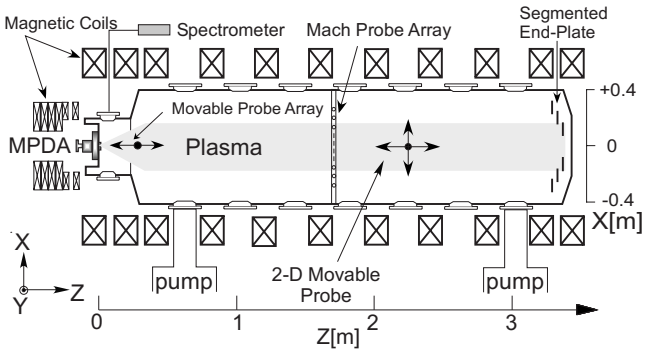

FIG. 1. Schematic of the HITOP device.

B. Spectroscopic measurement of the ion temperature and flow velocity

The spectroscopic method was used for measuring the ion temperature T_i, and the axial and rotational flow velocities u_z and u_θ, in the outlet region of the MPDA. The ion temperature and flow velocities were obtained from the Doppler broadening and the spectral shift of line spectra. For helium plasma, the He II line ($\lambda=468.58$ nm) is used to measure T_i, u_θ, and u_z; it is detected by means of a Czerny-Turner spectrometer with a focal length of 1 m and a grating mirror of 2400 grooves/mm, where a CCD camera coupled to an image intensifier is set at the exit plane of the spectrometer.[16] The line spectra are obtained at a spectral

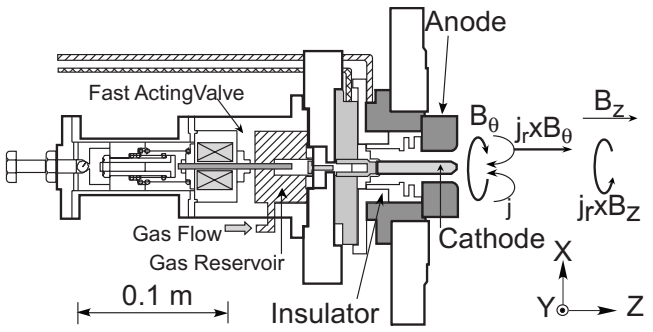

FIG. 2. Schematic of the MPDA and the direction of the Lorentz forces.

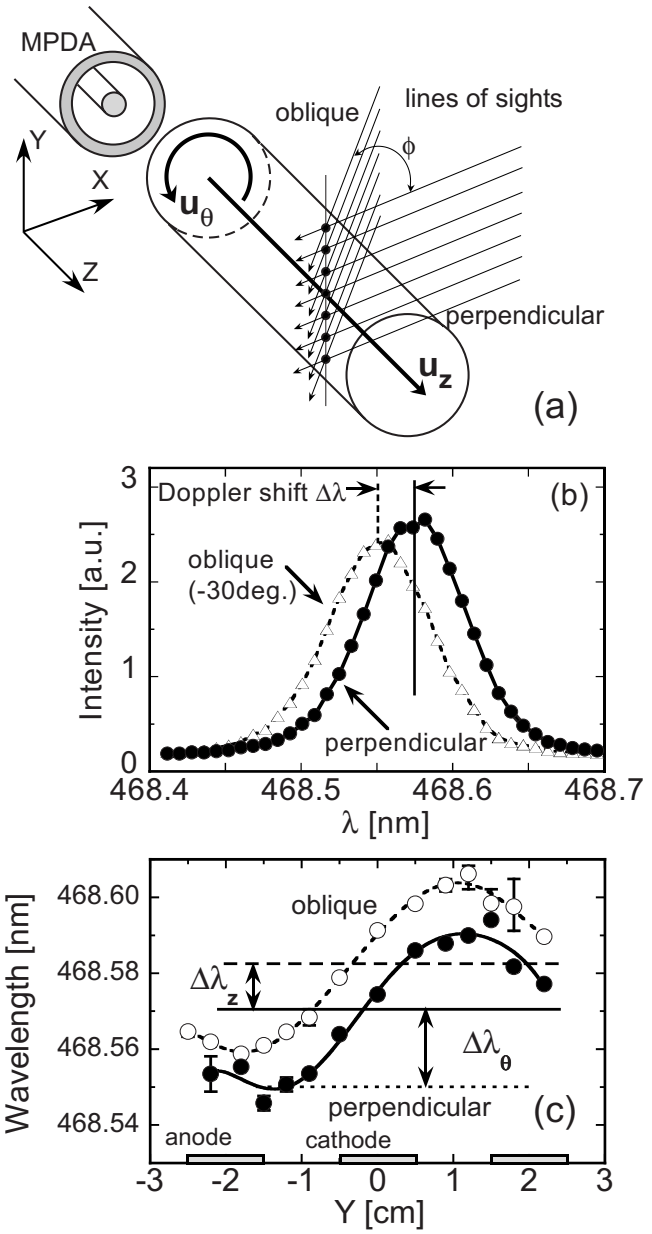

FIG. 3. (a) Schematic of the spectroscopic measurement of T_i, u_z, and u_θ. The spectrum lines were measured along the perpendicular and the oblique viewing lines. (b) Examples of the spectra measured along the perpendicular and the oblique viewing lines. (c) Radial profiles of the peak wavelengths of the measured spectra. The peak wavelengths shift due to the rotational flow (perpendicular view), and both the axial and the rotational flow (oblique view).

resolution of 0.02 nm. Light emission from the plasmas is viewed through a focusing camera lens and transmitted to the spectrometer by a 10 m optical fiber. Spatial resolution at the measurement position is 2 mm. The viewing angle and position of the focusing lens are changed shot by shot. In spectroscopic measurement, the lines of sights were set as shown in Fig. 3(a). The radial profiles of the line spectra were measured perpendicularly and obliquely to the plasma column. Each line spectrum was affected by the Doppler broadening, depending on the ion temperature and the Doppler shift due to both the axial and azimuthal motion of the He ions. Examples of measured spectra of He II line are shown in Fig. 3(b). The obtained profile was fitted as a Gaussian profile and an ion temperature was obtained by line broadening $\Delta\lambda_{1/e}$ as $T_i=(m_ic^2/2k_B\lambda_0^2)\Delta\lambda_{1/e}^2$. Here, c is the velocity of light and m_i is the mass of ions. The effect of spectrometer slit width on the line broadening was also considered. The flow velocity u is calculated as $u=c\Delta\lambda/(\lambda_0 \sin\phi)$ using the spectral shift $\Delta\lambda$ of the peak from that observed perpendicularly. The data points in Fig. 3(b) were those obtained by the CCD camera's pixels. The shift of one pixel corresponds to the flow velocity of 5.2 km/s. Figure 3(c) shows the radial profiles of the peak wavelength for each line of sight. In order to eliminate the measurement error, we measured the spectra three or five times at each position and the averaged data are plotted in the figure with error bars, which indicate how the data are scattered. No error bars can be distinguished at the center region because of the good reproducibility of the plasma; in contrast, the data in the peripheral region are scattered due to weak emission intensity. In the perpendicular measurement, the radial profile of the rotational velocity (u_θ) was estimated by evaluating the spectrum shift ($\Delta\lambda_\theta$) from the center of the profile at each position. The ion temperature was also derived from each spectrum line broadening. As the spectral emission comes from excited ions on the line of sight, the measured spectra are affected by superfluous emission. We assumed that the spectral shift and broadening are induced mainly by the ions at the center, because of their larger emission intensity. The emission from peripheral region contributes not to main peak shift but to line broadening, since the shifted value is smaller than that from the center position. The axial flow velocity (u_z) was derived from the difference between the center wavelengths of two radial profiles of the line spectrum ($\Delta\lambda_z$) obtained by viewing perpendicular and oblique viewing angle, as shown in Fig. 3(c). Even though u_z was derived from the line-averaged velocity along the line of sight, wavelength of Doppler shift ($\Delta\lambda_z$) in the spectrum was almost constant at each radial position, which indicates that u_z was almost uniform in the radial direction in the core plasma region. The derived axial velocity is also affected by superfluous emission from different axial positions. The inclination angle of the viewing line is limited to the range of 60° to 90° to the Z axis because of the limitation of the window size. The error of the axial position is limited to 3 cm, considering the plasma diameter of 5 cm. We assumed that the radial profiles of the axial and azimuthal velocity of the plasma were almost constant within the small axial distance. As the u_z is derived using more than 100 shots at each axial position in order to obtain the radial profile similar to Fig. 3(c), each u_z is an averaged value in these shots. The shift of 0.01 nm corresponds to 6.4 km/s in viewing parallel to the flow. The error of the estimation of u_z is not so large, although we cannot draw the error bar in the normal statistical way.

C. Measurement of the magnetic field and current density in a plasma flow

Time-varying magnetic fields in the electromagnetically accelerated plasma flows were measured directly using a movable magnetic probe array. It consists of 11 magnetic

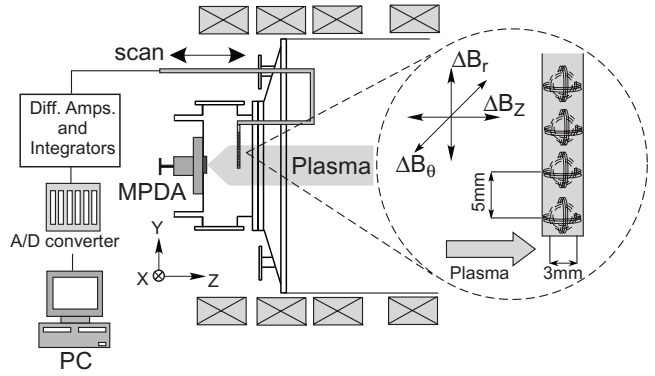

FIG. 4. Schematic of the multi-channel magnetic probe array and data acquisition system.

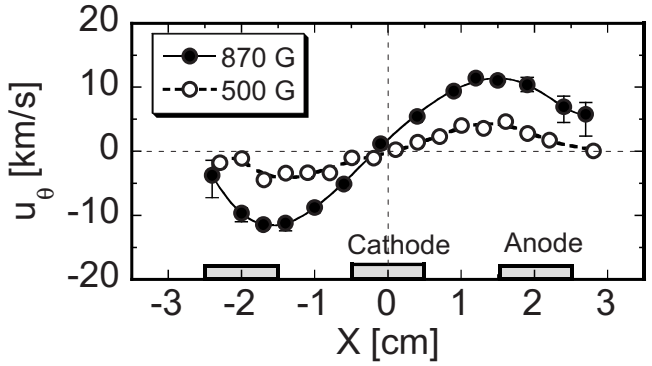

FIG. 5. Radial profiles of the rotational velocity in the applied field B_z of 870 G (solid circles) and 500 G (open circles). I_d=7.2 kA, Z=9 cm.

probes arrayed in the radial direction every 5 mm as shown in Fig. 4. Each probe has three sets of mutually perpendicular pick-up coils to measure three components of the magnetic field variation: ΔB_r, ΔB_θ, and ΔB_z. The probe signals (B-dot signals) are transferred to differential amplifiers and integrators and digitized at 1 M samples per second. The spatial profile of current density flowing in the plasma also evaluated from the Maxwell's equation, i.e., $\mu_0 \boldsymbol{j}=\mathrm{rot}\,\boldsymbol{B}$, using the measured three components of the magnetic field. Assuming that the spatial profiles are axisymmetric, the current density can be calculated from the observed magnetic field, as follows:

$$j_r = -\frac{1}{\mu_0}\frac{\partial B_\theta}{\partial z}, \tag{1}$$

$$j_\theta = \frac{1}{\mu_0}\left(\frac{\partial B_r}{\partial z} - \frac{\partial B_z}{\partial r}\right) \approx -\frac{1}{\mu_0}\frac{\partial B_z}{\partial r}, \tag{2}$$

$$j_z = -\frac{1}{\mu_0 r}\left(B_\theta + r\frac{\partial B_\theta}{\partial r}\right). \tag{3}$$

Here, the first term of Eq. (2) was eliminated because the ratio $[(\partial B_z/\partial r)/(\partial B_r/\partial z)]$ was larger than 100 in our experiments. We derived the spatial profiles of the Lorentz force, i.e., $\boldsymbol{F}=\boldsymbol{j}\times\boldsymbol{B}$, from the obtained $\boldsymbol{B}$ and $\boldsymbol{j}$ fields.

III. EXPERIMENTAL RESULTS AND DISCUSSIONS

A. Plasma rotation in an axial magnetic field

The characteristics of the azimuthal plasma flow near the outlet of the applied-field MPDA were investigated spectroscopically. Figure 5 shows the radial profiles of the azimuthal flow (rotational) velocity u_θ in a uniform applied-field B_z of 870 and 500 G at helium mass flow rate dm/dt of 0.1 g/s. The u_θ value increased linearly with the radius up to the inner radius of the anode (core region); that is, the angular frequency ω was constant in the core region. This indicates that the plasma column rotates as a rigid body. The rotational velocity increases with an increasing B_z.

In the MPDA, an inward electric field was formed due to the electrode configuration of the center cathode and the annular anode. Although the direction of plasma rotation corresponded to that of the $E\times B$ drift, the dependence of u_θ on the applied-field strength contradicted with the dependence $v_{E\times B}=E_r/B_z$ in the $E\times B$ drift. As the plasma rotation was not determined based on the $E\times B$ drift only, we went on to clarify the physical mechanism of plasma rotation in the applied-field MPDA.

We attempted to formulate the equilibrium of the rotational plasma column near the outlet of the MPDA.[16] The radial component of the equation of motion is expressed as follows:

$$m_i n_i\left(\frac{u_\theta^2}{r}\right) - \left(\frac{\partial p}{\partial r}\right) + j_\theta B_z - j_z B_\theta = 0, \tag{4}$$

where p is the plasma pressure re-expressed as $p=p_i+p_e=k_\mathrm{B}(n_iT_i+n_eT_e)$. The radial component of the generalized Ohm's law is expressed as follows:

$$en_i(E_r + u_\theta B_z - u_z B_\theta) - (j_\theta B_z - j_z B_\theta) + \frac{\partial p_e}{\partial r} = 0. \tag{5}$$

From these equations, u_θ is expressed as follows:

$$u_\theta = -\frac{E_r}{B_z} + u_z\frac{B_\theta}{B_z} - \frac{m_i u_\theta^2}{erB_z} + \frac{k_\mathrm{B}T_i}{eB_z}\frac{\partial \ln n_i}{\partial r}. \tag{6}$$

Here, T_i was assumed to be constant radially, which was confirmed by the experiments. The terms on the right-hand side of Eq. (6) correspond to the $E\times B$ drift, the effect of a helical stream line attributed to the helical magnetic field formed by B_z and B_θ, the centrifugal force drift, and the ion diamagnetic drift, respectively. As the measured radial intensity profile of the He II line emission was Gaussian,[16] the ion density profile was assumed to be Gaussian, and is expressed as $n_i(r)=n_0\exp[-(r/r_0)^2]$. E_r from Eq. (6) can then be expressed as follows:

$$E_r = -\frac{2r}{r_0^2}\frac{k_\mathrm{B}T_i}{e} - \frac{m_i u_\theta^2}{er} - (u_\theta B_z - u_z B_\theta). \tag{7}$$

The plasma column rotates azimuthally as a result of a balance among the $E\times B$ drift, the effect of the helical stream line, the centrifugal force drift, and the ion diamagnetic drift. These equations are similar to those in Ref. 16. The B_θ term, however, was neglected, and B_z was assumed to

be constant in the plasma because there was no precise measurement of the magnetic fields near the MPDA in the calculation of Ref. 16.

We calculated the electric field according to Eq. (7) using the ion temperature and velocity measured by spectroscopy and the magnetic fields measured by magnetic probes. The potential profiles in the plasma were also calculated and are shown in Fig. 6 as dotted and solid lines at B_z of 500 and 870 G, respectively, assuming that $\phi_s=0$ V at $X=\pm 3$ cm. In order to confirm the evaluation of E_r experimentally, we compared the potential profile calculated using Eq. (7) with the measured one. As ϕ_s could not be measured directly by a Langmuir probe because of the high-density plasma near the MPDA (more than 10^{21} m^{-3}), we measured the radial profile of the floating potential ϕ_f near the outlet of the MPDA ($Z=9$ cm) and plotted it, as shown in Fig. 6. Difference in the absolute values of ϕ_f and ϕ_s depends on the electron temperature T_e as $\phi_s-\phi_f=(kT_e/e)\ln(0.657\sqrt{m_i/m_e})\approx 4T_e(\mathrm{eV})$ in helium. We measured the radial profile of T_e at 50 cm downstream from the MPDA and found that T_e is almost constant around 5 eV in the radial direction. We also measured an axial profile of T_e, and this gradually decreases from 5 to 4 eV along with the flow direction. These observations indicated that the electron temperature could be estimated at constant. We assumed that T_e was almost constant in radial profile, as well as the radial profile of T_i, which was spectroscopically confirmed, and that the shape of radial profile of ϕ_f was similar to that of the plasma potential ϕ_s. Both the measured potential profiles at B_z of 500 and 870 G were parabolic and in good agreement with the calculated profiles. The ratio of the four drift components in Eq. (6) was 1:0.13:0.06:0.64. Although the $E\times B$ drift was dominant and the direction of the plasma rotation corresponded to that of the $E\times B$ drift, the applied-field MPDA plasma rotated as a rigid body due to the combination of these drifts. It was also confirmed experimentally that the on-axis plasma potential drop becomes large and the radial electric field increases at higher applied-field strengths.

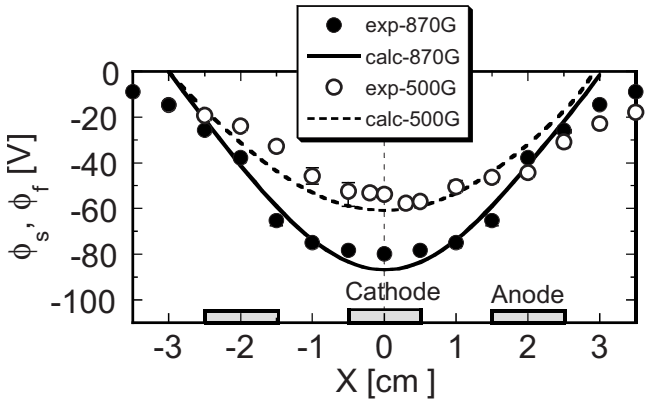

FIG. 6. Comparison of the measured floating potentials (solid and open circles) and calculated space potential (solid and dashed curves).

B. Axial profile of M_i and the saturation phenomena related to the Mach number

In the discharge region of the MPDA, where the discharge current concentrates, joule heating is expected to occur in addition to the direct acceleration induced by the axial Lorentz force. Plasma heating induced by plasma viscosity is also expected. Therefore, a comparison between the flow energy and the thermal energy is useful for evaluating the acceleration performance.

The ion acoustic Mach number M_i is one of the important parameters of accelerated flows, and is defined by the following equation:

$$M_i=\frac{u}{\sqrt{\frac{k_\mathrm{B}(\gamma_e T_e+\gamma_i T_i)}{m_i}}}. \tag{8}$$

Here, k_B is Boltzmann's constant, m_i is the ion mass, and γ_i and γ_e are the specific heat ratios of ions and electrons, respectively. The square of Ma_i is related to the ratio of flow energy to thermal energy of the flowing plasma. We evaluated M_i in plasmas with measured velocities and temperatures. In the externally applied field, plasma flows axially and azimuthally. Hence, M_i is calculated using the total velocity defined as $u_\mathrm{total}=\sqrt{u_z^2+u_\theta^2}$. The electron temperature T_e was measured in the downstream region, more than 50 cm apart from the MPDA, by a Langmuir probe with fast-sweeping of the bias voltage during a discharge and the obtained T_e was typically 5 eV.

In the calculation of the Mach number, we have used the specific heat ratios of ions and electrons; i.e., $\gamma_i=5/3$ and $\gamma_e=1$, respectively. The specific heat ratio of ions γ_i was evaluated experimentally from the spatial change of M_i in a diverging magnetic field. In a large-scale diverging magnetic nozzle, γ_i was estimated to be 1.2, which is less than the value of 5/3 in an ideal mono-atomic ion gas. The plasma parameters in the Ref. 15, however, differ from the present data obtained near the MPDA outlet. Although the evaluation of the specific heat ratio is an important and still ongoing task, we simply adopted the $\gamma_i=5/3$ in the present calculation of M_i, assuming that ions behave as an ideal monoatomic gas in the present calculation of M_i. As the thermal velocity of electrons is much higher than that of ions, we assumed that electron motion is isothermal and used as $\gamma_e=1$ the specific heat ratio of electrons.

Figure 7 shows the dependencies of u_z, u_θ, T_i, and M_i on the discharge current I_d, in a uniform applied field of 870 G at a helium mass flow rate dm/dt of 0.1 g/s. Both u_z and u_θ increased almost linearly with I_d. T_i also increased with I_d and increased steeply when I_d was higher than 8 kA. Consequently, M_i saturates less than unity near the outlet region of the MPDA.

In Fig. 7 and the subsequent figures, there is no error bar for the axial velocity u_z, and consequently for M_i, which is calculated using u_z. As mentioned in Sec. II, the evaluation of u_z requires more than 100 shots for each measurement point. The data for u_z and M_i were averaged over these shots. The flow velocity in the radial direction (u_r) in the plasma

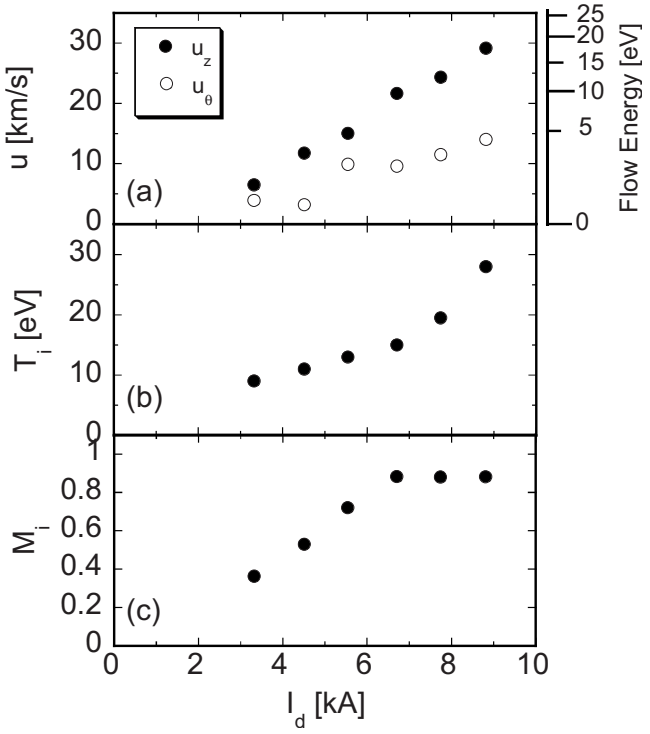

FIG. 7. Dependencies of (a) u_z and u_θ, (b) T_i, and (c) M_i on the discharge current I_d. B_z=870 G and the mass flow rate of helium, i.e., dm/dt =0.1 g/s, measured at Z=30.5 cm. Ma_i was calculated assuming the specific heat ratios of ions and electrons, i.e., γ_i and γ_e, of 5/3 and 1, respectively.

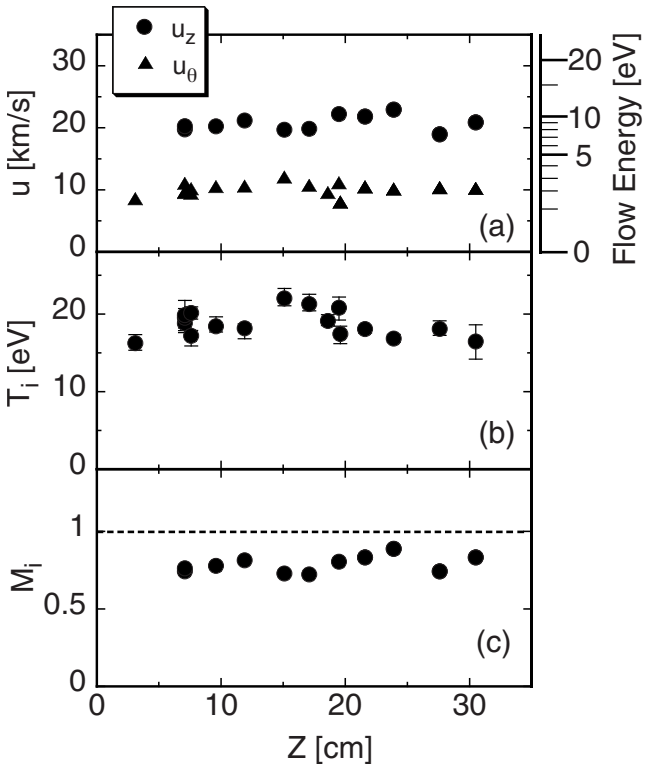

FIG. 9. Axial profiles of (a) u_z and u_θ, (b) T_i, and (c) M_i. I_d=7.2 kA, B_z =870 G, and dm/dt=0.1 g/s. Ma_i was calculated assuming the specific heat ratios of ions and electrons, i.e., γ_i and γ_e, of 5/3 and 1, respectively.

was considerably small, since the plasma radius estimated from emission profile was almost constant along the z axis.

Figure 8 shows the axial profile of T_i for various discharge currents. In a high-current regime, T_i increased drastically in the slightly downstream region, especially around Z=10 cm or more. When I_d was more than 8 kA, T_i increased twofold. It was indicated that the input electric power tends to be converted into thermal energy rather than plasma flow energy. As a result, u_z in the downstream region was almost constant or slightly decreased in a uniform magnetic field, as shown in Fig. 9. This indicates that the Mach number is saturated at a value less than unity in the case of uniform magnetic fields, and that the plasma thermal energy becomes larger than the flow energy.

In order to improve the acceleration performance, the saturation phenomena of M_i should be avoided. As the electromagnetic force predominates in the plasma in addition to aerodynamic effects, M_i is expected to increase upon optimizing the magnetic field configuration. We evaluated the electromagnetic force experimentally in order to clarify the MPDA plasma behavior in applied-magnetic field and to optimize the magnetic field configuration.

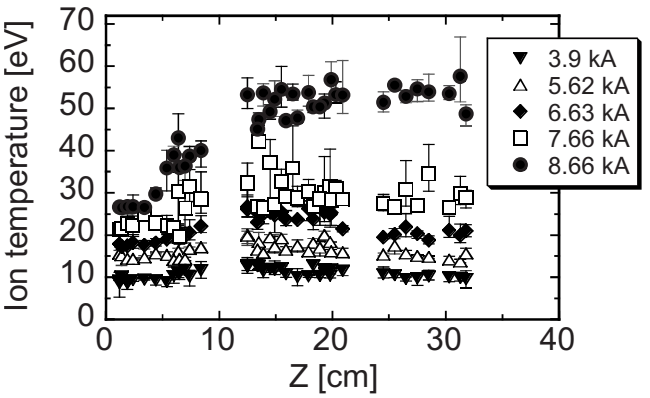

FIG. 8. Axial profiles of the ion temperature for various discharge currents measured along the line of sight at Y=0. B_z=1 kG, dm/dt=0.06 g/s.

C. Evaluation of the Lorentz force in the MPDA plasma flow

We measured the spatial profiles of three components of the magnetic field in the MPDA plasma flow using a multichannel magnetic probe array.[19] The spatial profiles of the magnetic field in conjunction with Eqs. (1)–(3) give us the plasma current density distributions, and then we can evaluate the spatial distribution of the Lorentz force working on the MPDA plasma. The time evolution of the axial variation of B_z on the axis of the plasma at Z=19 cm is shown in Fig. 10. The net axial magnetic field decreases due to the diamagnetic effect of the high-density MPDA plasma.

The radial profile of the three components of the magnetic field in a uniform applied field of 870 G is shown in Fig. 11. It is remarkable that the net field strength B_z is reduced to half at the center of the plasma. This large diamagnetic effect is caused by a high beta condition near the

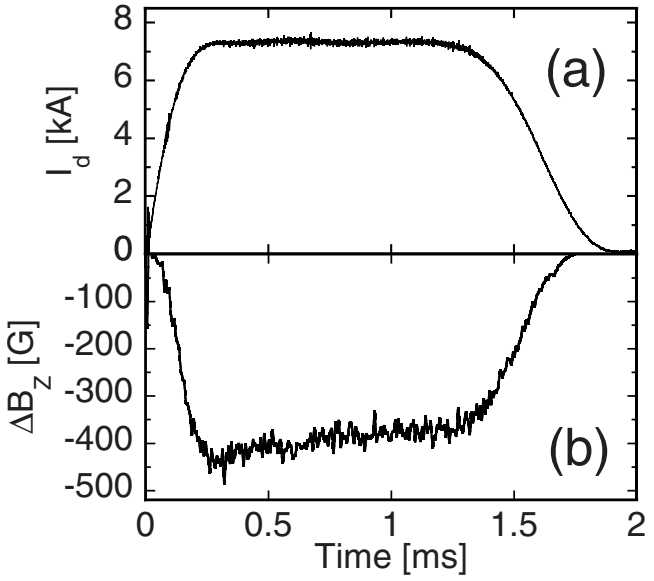

FIG. 10. Typical time evolutions of (a) the discharge current and (b) the diamagnetic signal on the axis at $Z=19$ cm. $I_d=7.2$ kA, $B_z=870$ G, and $dm/dt=0.2$ g/s.

MPDA. The decrease in B_z is related to the plasma pressure, $p=n_e k_B(T_e+T_i)$, via the following simple pressure balance equation:

$$p=\frac{B_{z0}^2-B_z^2}{2\mu_0}. \tag{9}$$

Here, B_z and B_{z0} are the magnetic field strengths, one with and the other without the plasma, respectively. In general, the plasma beta value is defined as $\beta=(2\mu_0 p/B_z^2)$. Thus, the ratio of $\Delta B_z/B_{z0}=(B_{z0}-B_z)/B_{z0}$ is also related to the β value as follows:

$$\beta=\frac{p}{(B_z^2/2\mu_0)}=\frac{B_{z0}^2-B_z^2}{B_z^2}=[1+(\Delta B_z/B_z)]^2-1. \tag{10}$$

When the magnetic field falls to half, the β value becomes larger than unity, and that occurred in the outlet region of the MPDA.

The azimuthal component of the magnetic field B_θ is induced by the axial plasma current, which is extended downstream along with the plasma flow. The axial profiles of

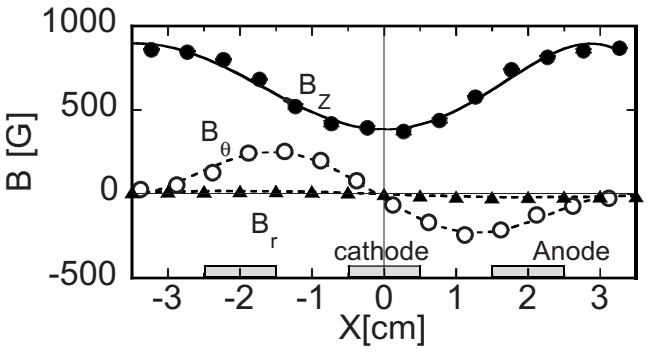

FIG. 11. Radial profiles of the three components of the magnetic fields measured at $Z=7$ cm. $I_d=7.2$ kA, $B_z=870$ G, and $dm/dt=0.1$ g/s.

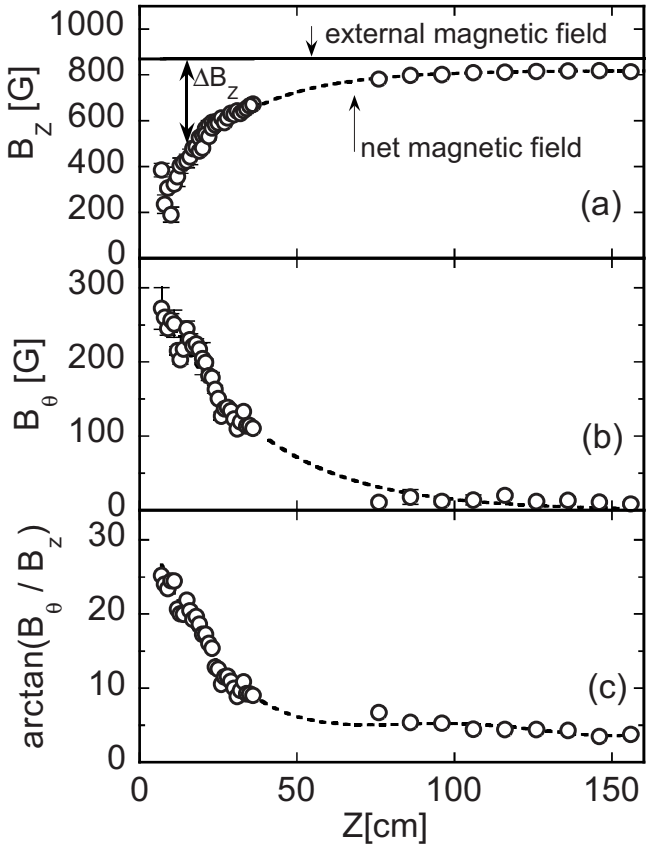

FIG. 12. Axial profiles of (a) the net axial field strength B_z, (b) the azimuthal field B_θ, and (c) arctan(B_θ/B_z). $I_d=7.2$ kA, $B_z=870$ G, and $dm/dt=0.1$ g/s.

the net field strength B_z, B_θ, and arctan(B_θ/B_z), are shown in Fig. 12. Here, arctan(B_θ/B_z) indicates the pitch angle of the helical magnetic field line and is calculated using the value at $X=-1.5$ cm, where B_θ is at its maximum. Owing to the diamagnetic effect, the net magnetic flux tube converges gradually. A slightly converging helical magnetic nozzle with a variable pitch is spontaneously formed, even though a uniform magnetic field is applied.

Figures 13(b)–13(d) show two-dimensional (2D) vector plots of the radial-axial components of the magnetic field, i.e., B_r and B_z, the plasma current densities j_r and j_z, and the Lorentz force fields F_r and F_z, respectively. The spatial profile of j_θ is also shown in Fig. 14. Here, the plasma current density is calculated using the Maxwell's equations rot $\boldsymbol{B}=\mu_0\boldsymbol{j}$ under the assumption of axisymmetry [see Eqs. (1)–(3)] and the Lorentz forces are calculated as $\boldsymbol{F}=\boldsymbol{j}\times\boldsymbol{B}$.

In the formula $F_z=j_r B_\theta - j_\theta B_r$, the second term, i.e., $-j_\theta B_r$, corresponds to the interaction between j_θ and B_r generated in the resultant converging magnetic field. This term acts as a deceleration force in the converging magnetic field and cancels the acceleration force of the first term; i.e., $j_r B_\theta$. The obtained force in the uniform applied field works to decelerate the plasma as shown in Fig. 13(d). This is one of the possible reasons that M_i is always below unity in the case of a uniform applied magnetic field.

In order to improve the plasma acceleration, the sign of B_r of the $-j_\theta B_r$ term should be reversed by applying a di-

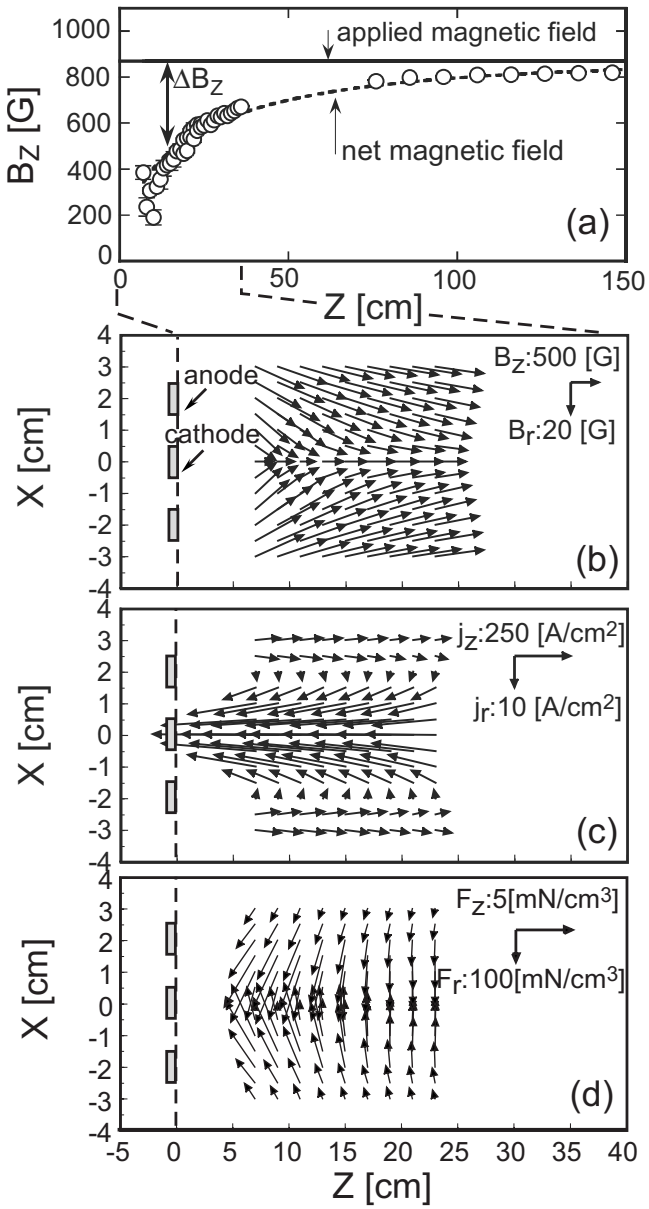

FIG. 13. (a) Axial profiles of the net axial field strength B_z, and 2D vector plots of (b) the magnetic field, (c) the plasma current density, and (d) the Lorentz force in the uniform applied field. The scales of reference vector interpolated in the figure are (b) B_z and B_r of 500 and 20 G, respectively; (c) j_z and j_r of 250 and 10 A/cm^2, respectively; and (d) F_z and F_r of 5 and 100 mN/cm^3, respectively. Although the radial component of the magnetic field is much smaller than that of the axial component, the spontaneously formed magnetic field is slightly convergent. The externally applied magnetic field B_z, is uniform at 870 G. I_d=7.2 kA, B_z=870 G, and dm/dt =0.1 g/s.

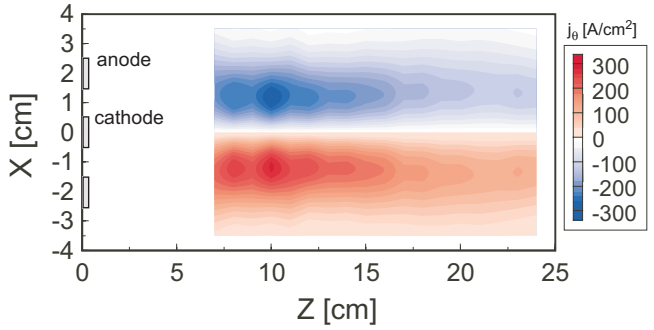

FIG. 14. (Color online) Contour plot of the azimuthal plasma current j_θ in the X-Z plane in the uniform applied field.

verging magnetic field externally. Figure 15(a) shows an externally applied diverging field and the measured net field strength. Even though a converging nozzle is still formed by the strong diamagnetic effect in the upstream region, it converts to a diverging field in the downstream region, where the diamagnetic effect decreases gradually; i.e., a magnetic Laval nozzle is spontaneously formed. The spatial distribution of the Lorentz forces in the externally applied diverging magnetic field is shown in Fig. 15(d). It is noteworthy that the direction of F_z converts from negative to positive in the region where the net magnetic flux tube changes from a converging one to a diverging one. This result shows that the Lorentz force distribution in the MPDA plasma can be controlled by adjusting the configuration of the externally applied field.

Beside the electromagnetic forces acting on plasmas, aerodynamic effects are also important in the behavior of flowing plasma in a magnetic field. The axial profiles of the Hall parameter of ions ($\omega_{ci}\tau_{ii}$) and electrons ($\omega_{ce}\tau_{ei}$) near the outlet region of the MPDA in the uniform applied field are shown in Fig. 16. Here, ω_{ci} and ω_{ce} are the ion and electron cyclotron frequencies, respectively, and τ_{ii} and τ_{ie} are the ion-ion and electron-ion collision times, respectively. These values correspond to the numbers of cyclotron motion between collisions. The electron Hall parameter is larger than unity, which means the electrons are magnetized. On the other hand, the ion Hall parameter is in the order of 10^{-1}. This indicates the ions are unmagnetized and behave as an ion fluid flowing along the magnetic field lines, since the electrons are magnetized and restricted to the field lines. In a conventional compressible gas dynamics, a Laval nozzle can effectively accelerate a subsonic flow to a supersonic one by converting thermal energy into flow energy. Therefore, for more efficient plasma acceleration, the magnetic Laval nozzle should be shaped appropriately, taking into account the diamagnetic deformation of the magnetic field. The effect of the magnetic Laval nozzle has been experimentally investigated and the supersonic plasma flow with $M_i > 1$ has been obtained successfully.[20]

It is also noted that the inward radial component of the Lorentz force, i.e., F_r (pinch force), is much larger than the axial component, i.e., F_z, in the measured region. This suggests that a pressure gradient arises from the pinch force near the outlet region, resulting in the enhancement of the axial plasma flow.

Both the electromagnetic force and these aerodynamic effects should be considered when optimizing the configuration of the externally applied magnetic field. This is an ongoing, crucial task for the further progress of plasma acceleration research.

IV. CONCLUSION

The spatial profiles of the plasma flow field and the electromagnetic field near the outlet of the MPDA were measured experimentally. The exhausted MPDA plasma rotates

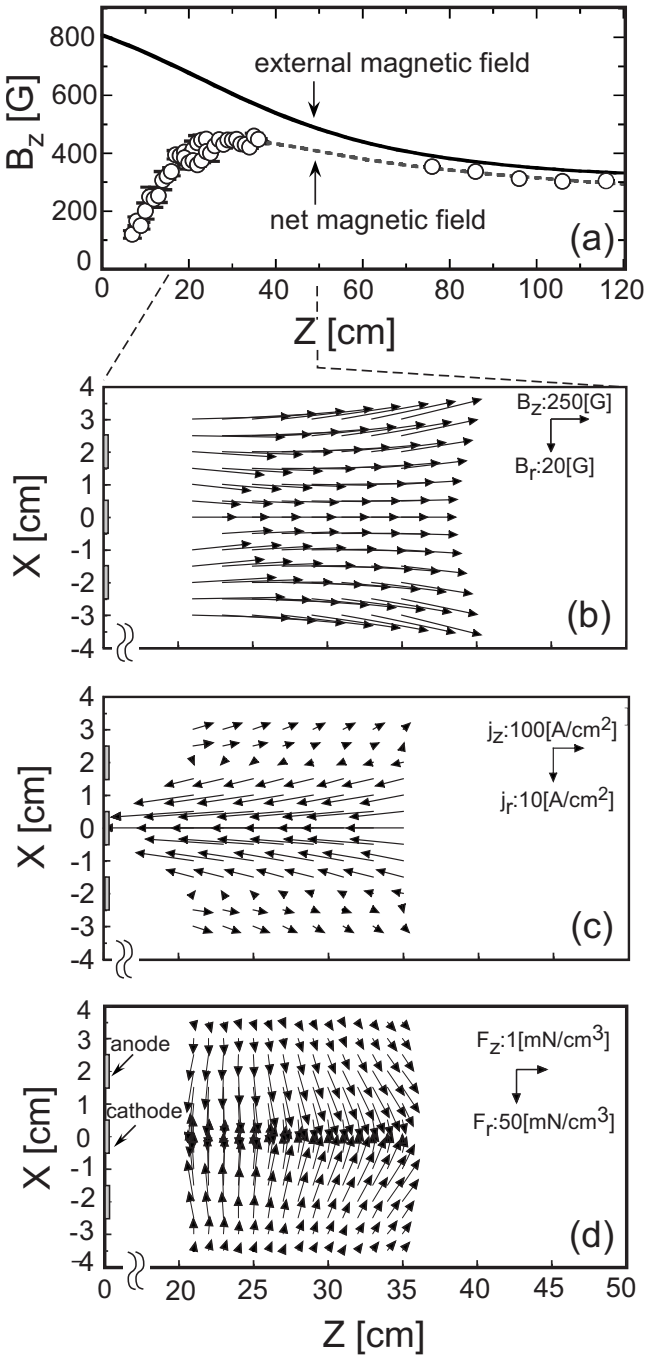

FIG. 15. (a) Axial profiles of the net axial field strength B_z and 2D vector plots of (b) the magnetic field, (c) the plasma current density, and (d) the Lorentz force in the diverging applied field. The scales of reference vector interpolated in the figure are (b) B_z and B_r of 250 and 20 G, respectively; (c) j_z and j_r of 100 and 10 A/cm^2, respectively; and (d) F_z and F_r of 1 and 50 mN/cm^3, respectively. I_d=7.2 kA and dm/dt=0.1 g/s.

azimuthally as a rigid body in an applied magnetic field. Considering the radial force balance of the plasma column, the plasma rotates azimuthally as a result of the balance among the $E\times B$ drift, the effect of the helical stream line, the centrifugal force drift, and the ion diamagnetic drift. The measured potential profile corresponds well to the theoretical evaluation.

In a high-current regime, the ion acoustic Mach number of the plasma flow is limited to a value less than unity due to a steep increase in T_i. To clarify the mechanism behind the Mach number saturation and improve the acceleration performance of the applied-field MPDA plasma, the spatial profiles of the magnetic field were measured and current densities and Lorentz forces acting on the plasma are evaluated. It was found that the high-beta plasma generated in the outlet of the MPDA significantly diminishes the external magnetic field by the diamagnetic effect, and that a converging helical magnetic nozzle with a variable pitch is spontaneously formed. The axial component F_z is weakened by a deceleration force due to the inward component B_r. It was demonstrated experimentally that the deceleration force could be converted to an acceleration force by applying a diverging magnetic field.

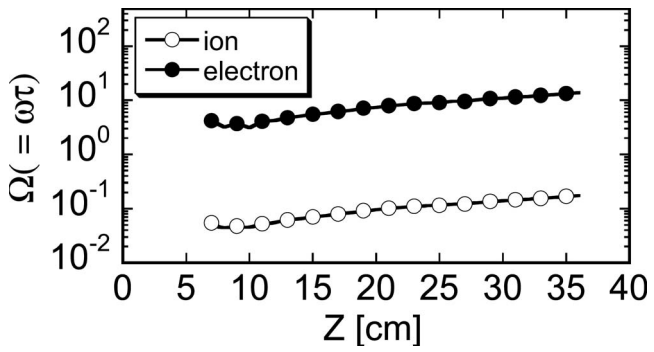

FIG. 16. Axial profiles of the ion (open circles) and electron (solid circles) Hall parameter. I_d=7.2 kA, B_z=870 G, and dm/dt=0.1 g/s.

The inward radial component of the Lorentz force, i.e., F_r (pinch force), was much larger than the other components. The pressure gradient near the outlet region also generates an axial plasma flow. For more efficient plasma acceleration, the shape of the applied magnetic field should be optimized by taking into account both the electromagnetic force and the aerodynamic effects. A magnetic Laval nozzle is one of the feasible candidates for the realization of an optimized applied-field MPDA.

[1] H. Xia, M. G. Shats, and H. Punzmann, Phys. Rev. Lett. **97**, 255003 (2006).
[2] R. G. Jahn, *Physics of Electric Propulsion* (McGraw-Hill, New York, 1968).
[3] H. Kuninaka and S. Satori, J. Propul. Power **14**, 1022 (1998).
[4] A. C. Ducati, G. M. Giannini, and E. Muehlberger, AIAA J. **2**, 1452 (1964).
[5] N. M. Nerheim and A. J. Kelly, "A critical review of the magnetoplasmadynamic (MPD) thruster for space application," Technical Report 32-1196, Jet Propulsion Laboratory, California Institute of Technology, 1968.
[6] A. C. Malliaris, R. R. John, R. L. Garrison, and D. R. Libby, "Quasi-steady MPD propulsion at high power," NASA CR-111872, 1971.
[7] R. K. Seal and H. A. Hassan, AIAA J. **6**, 2273 (1968).
[8] G. Krülle, in *Proceedings of AIAA 9th Electric Propulsion Conference*, Bethesda, MD (AIAA, New York, 1972), AIAA Paper 72–501.
[9] M. Tanaka and I. Kimura, J. Propul. Power **4**, 428 (1988).
[10] A. Sasoh and Y. Arakawa, J. Propul. Power **8**, 98 (1992).
[11] H. Tahara, Y. Kagaya, and T. Yoshikawa, J. Propul. Power **11**, 337 (1996).
[12] H. Tahara, Y. Kagaya, and T. Yoshikawa, J. Propul. Power **13**, 651 (1997).
[13] G. Krülle, M. A. Krutz, and A. Sasoh, J. Propul. Power **14**, 754 (1998).
[14] A. Ando, A. Imasaki, H. Tobari, T. Yagai, K. Hattori, and M. Inutake, Trans. Fusion Technol. **43**, 130 (2003).
[15] M. Zuin, R. Cavazzana, E. Martines, G. Serianni, V. Antoni, and M. Bagatin, Phys. Rev. Lett. **92**, 225003 (2004).
[16] A. Ando, M. Ashino, Y. Sagi, M. Inutake, K. Hattori, M. Yoshinuma, A.

Imasaki, H. Tobari, and T. Yagai, J. Plasma Fusion Res. **4**, 373 (2001).
[17]M. Inutake, A. Ando, K. Hattori, H. Tobari, and T. Yagai, J. Plasma Fusion Res. **78**, 1352 (2002).
[18]M. Inutake, A. Ando, K. Hattori, T. Yagai, H. Tobari, R. Kumagai, H. Miyazaki, and S. Fujimura, Fusion Sci. Technol. **43**, 118 (2003).
[19]H. Tobari, M. Inutake, A. Ando, and K. Hattori, J. Plasma Fusion Res. **80**, 651 (2004).
[20]M. Inutake, A. Ando, K. Hattori, H. Tobari, T. Makita, M. Shitaba, Y. Kasashima, and T. Komagome, Plasma Phys. Controlled Fusion **49**, A121 (2007).